Modeling and Validation for Performance Analysis and Impedance Spectroscopy Characterization of Lithium-Ion Batteries

Jin Zhao[a], Jaber A. Abu Qahouq[a]

[a]*Department of Electrical and Computer Engineering, The University of Alabama, Box 870286, Tuscaloosa, 35487-0286, AL, USA*

Abstract

A parameterized mathematical model for Lithium-ion battery cell is presented in this paper for performance analysis with a particular focus on battery discharge behavior and electrochemical impedance spectroscopy profile. The model utilizes various physical properties as input and consists of two major sub-models in a complementary manner. The first sub-model is an adapted Doyle-Fuller-Newman (DFN) framework to simulate electrochemical, thermodynamic, and transport phenomena within the battery. The second sub-model is a calibrated solid-electrolyte interphase (SEI) layer formation model. This model emphasizes the electrical dynamic response in terms of the reaction process, layer growth, and conductance change. The equivalent circuit component values are derived from the outputs of both sub-models, reflecting the battery's changing physical parameters. The simulated discharge curves and electrochemical impedance spectroscopy (EIS) profiles are then provided with a comparison against empirical results for validation, which exhibit good agreement. This modeling methodology aims to bridge the gap between the physical model and the equivalent circuit model (ECM), enabling more accurate battery performance predictions and operation status tracking.

Keywords: Li-ion battery, mathematical modeling, physics model, simulation and validation, EIS, ECM

Submitted to and Accepted by Next Energy Journal Submitted draft as of June 23, 2024

1. Introduction

The Li-ion battery (LIB) behavioral model can be constructed under various approaches such as learning-based methods [1, 2, 3, 4, 5], data-driven analysis [6, 7, 8], equivalent circuit model (ECM) characterization [9, 10], and via multiphysics platforms [11, 12, 13]. Despite these options, mathematical and parameterized physics models are considered in this paper, due to their inherent advantages such as more flexible, intuitive, and versatile in both implementation and adaptation. This model adapts the Doyle-Fuller-Newman (DFN) framework for cylindrical LIBs, specifically targeting 18650 type. It is to better match these batteries' distinct characteristics, focusing on their electrical and electrochemical features. The model provides steady-state performance predictions for batteries at acceptance, using ECM population and electrochemical impedance spectroscopy (EIS) for validation against public-domain battery data. Subsequent sections will detail the model's predictive capabilities for battery behavior at acceptance. However, due to its focus on steady-state behavior, the model is not equipped with aging tracking and analysis ability. Furthermore, discussions on enhancing battery life and performance primarily belong to the realms of metallurgical and material science research and are not addressed within the scope of this paper.

The DFN model is a generalized mathematical modeling approach for LIBs, focusing on predicting charging and discharge behaviors under galvanostatic conditions [14]. Doyle *et al.* presented the charge transport from the lithium anode to the composite cathode through a polymer membrane as a one-dimensional process, involving simultaneous lithium ion (Li^+) diffusion within the active materials[1] and electrolyte, charge transfer at the electrode/electrolyte interphase, and Li^+ migration within the electrolyte. This framework, since first introduced in 1993, has gained widespread acceptance and has been extensively modified for complex LIB modeling. Numerous research groups have contributed various revisions and enhancements to the original DFN framework, enriching its applicability and accuracy in advanced LIB studies. In [15], a DFN-based LIB model is developed emphasizing battery charge and

[1]The active material in a battery is the material that is electrochemically active. This is the material that participates in the chemical reactions that store and release energy in the battery.

discharge responses from simulation. The DFN model in [15] is reconfigured into a pseudo-two-dimensional (P2D) model in which solid particles are treated as 2D circles. This approach allows for a detailed examination of Li^+ diffusion and changes in particle concentration during charge and discharge processes at a micro-scale level. The P2D model demonstrates a reliable voltage profile and exhibits a qualified capability for parameter identification. Another noteworthy modeling approach is Python Battery Mathematical Modelling [16]. It is an open-source platform for the simulation and analysis of various battery types. With the sheer content of numerical methods and solvers for tackling the algebraic and differential equations associated with battery models, it facilitates comparisons among different modeling approaches, enabling researchers to investigate battery performance such as aging, charge/discharge curves, and thermal response. In [17], Wang *et al.* emphasized the flexibility of DFN model in capturing key microscopic mechanisms of battery operation, then introduced the LIB database that aggregates numerous parameters necessary for the DFN model. In [18], the integration of the DFN model with machine learning (ML) has been presented by Tu *et al.* to track and predict charge rates C_{rate} with certain accuracy. The DFN framework provides dynamic and state information from the physical model, which has fed into the ML model for behavior prediction. Last but not least, in [19], Lagnoni *et al.* proposed an electrolyte transport model within the DFN framework, comparing directly against the generic Nernst-Planck model. The proposed model accounts for the electrolyte behavior, especially on its implications on thermal effects. This model offered more details in LIB operation, which is a strong addition to the DFN framework.

This paper introduces a physics-based mathematical model specifically designed for analyzing the steady-state response of 18650 LIB at acceptance. Developed from a variant of the DFN framework and incorporating a range of physical parameters, the model has been implemented exclusively in MATLAB®. It enables the simulation of the battery's discharge process and provides a detailed analysis of its EIS characteristics [14, 20, 21].

In terms of performance analysis, a simplified representation of the solid-electrolyte interphase (SEI) layer is incorporated into the model to capture the formation process [22]. As part of the output, physical and electrochemical changes during simulation are then used to populate the ECM component values. Note that these component values are evaluated based on progressive LIB physical parameters and EIS characterization. For the steady-state model, the initial formation of SEI layer on electrodes

is carefully modeled, this is to address the Li^+ loss in the electrolyte. However, this paper does not cover the evolution of SEI layers as well as the corresponding irreversible chemical changes within a LIB. In turn, the SEI layer growth and evolution is recognized as the immediate next step for the authors.

The main contribution of this paper includes:

- A physics-based mathematical model, describing LIB steady-state behavior, is presented. The model intakes exhaustive initial battery parameters to build a 2D DFN model. The model is capable of including specific battery details and is flexible in adjusting parameters based on different battery features.
- The presented model exhibits the capability of predicting discharge curves and characterizing EIS profiles under varying charge rates and temperatures. The results obtained from the model are validated using NASA empirical data, as is shown in Section 4.

In the remainder of this paper, Section 2 provides a description of the LIB mathematical model and provides a comprehensive list of relevant battery parameters used in the model. Section 3 presents the model simulation results, illustrating battery behavior under various charge rates and temperatures. Section 4 explains the component value estimation process for the ECM, followed by the characterization of an EIS based on the ECM. Last but not least, Section 5 offers additional discussion on the presented model and concludes the paper.

2. Methods

A general implementation diagram of the presented physics-based LIB mathematical model is shown in Figure 1, which consists of four main stages:

- Stage 1: Prepare physical parameter values of LIB, including geometric, material, electrochemical, transport, *etc.*. Data can be obtained from public-domain datasets [44, 17], datasheets of specific tests [45, 46], and publications [47].
- Stage 2: Develop the basic battery model using 2D-DFN framework per the geometry and chemistry features for 18650 battery, for capturing the electrochemical processes during operation [15, 21, 48].

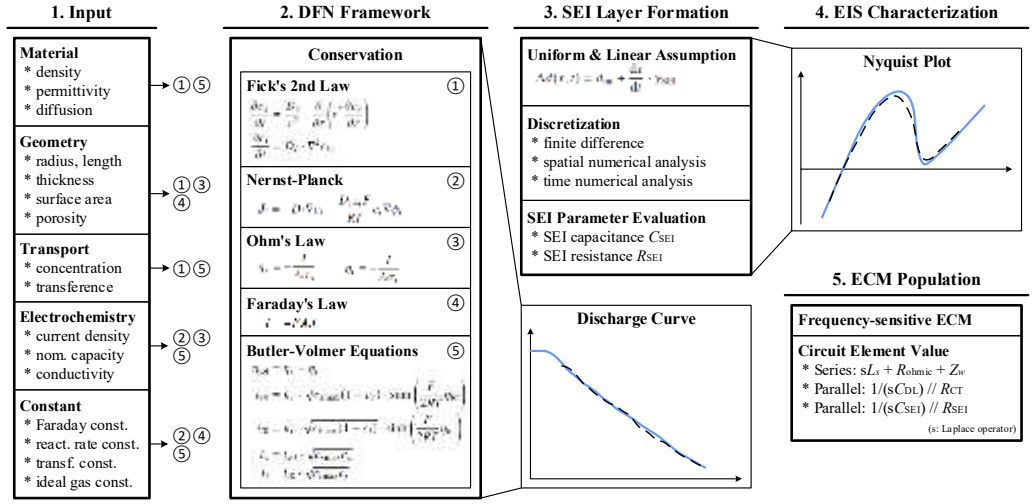

Figure 1: Comprehensive diagram of the LIB parameterized mathematical model implementation.

- Stage 3: Build the SEI formation model based on the progressive variables from DFN framework. Such variables include but are not limited to electrolyte diffusivity D_x, ionic conductivity σ_x, and ionic current density $\boldsymbol{J}$. The subscript x in this stage represents variables associated with either the positive (p) or negative (n) electrode.
- Stage 4: Simulate model for 1) battery discharge behavior under different C_{rate}; 2) EIS profile characterization by sweeping ambient temperature T; and 3) populate ECM component values. The simulation results are then validated by comparing against NASA test data.

Note that the model simulation employs MATLAB Particle Swarm Optimization (PSO) toolbox. PSO is widely used in battery modeling for various optimization tasks, including parameter estimation, model calibration, and battery design optimization. The formation of the SEI model entails certain foundational assumptions that will be explained in Section 2.2.

There are mainly three sub-models that are also described in Figure 1 and discussed in the next section: (1) DFN architecture, in Section 2.1, (2) SEI layer formation, in Section 2.2, and (3) ECM elements population based on EIS, in Section 4. The model output includes discharge curves, EIS profiles, and populated circuit element values. A comprehensive list of parameters and

Table 1: List of math symbols and descriptions of parameters and variables that appeared in the modeling process (part 1 of 2).

Class	Symbol	Description	Value	Unit
Geometry	A	electrode surface area	[23]	m^2
	A_s	active material surface area	[23]	m^2
	d_x	electrode thickness	[24, 25]	m
	l_x	unwrapped electrode length	[26]	m
	r	electrode radius	[24]	m
Material	ε_{DL}	double-layer rel. dielec. permit.	[27]	–
	ρ	resistivity of the material	[28]	$\Omega \cdot m$
	d_{DL}	double layer thickness	[29, 30]	m
	D_x	diffusion coefficient	[25]	m^2/s
	l	conductor length	[25, 31]	m
Electro-chemistry	η_x	overpotential	(5)(6)	V
	η_{tot}	total overpotential	(7)	V
	σ_x	ionic conductivity	[28]	S/m
	ϕ_e	electric potential	[23]	V
	i_{x0}	exchange current density	(8)(9)	A/m^2
	i_x	interphasal current density	(10)(11)	A/m^2
	I	current density distribution	(4)	A
	$\boldsymbol{J}$	ionic current density	(3)	A/m^2
	k_x	reaction rate constant	[25]	$m^{2.5}/mol^{0.5}/s$
	L_{area}	per unit-area inductance	[32, 33, 34]	H/m^2
	z_e	charge number	[35]	–
Transport	c_x	Li^+ concentration	(1)(2)	mol/m^3
	c_{xmax}	maximum concentration	[36]	mol/m^3

variables used in the model and their corresponding mathematical symbols are provided in Table 1 (2 parts total). The corresponding references or equations in this paper that provide related information are listed in the "Value" column of the table.

2.1. DFN Architecture

The presented DFN model architecture is a 2D representation, inspired and adapted by [15, 19, 49, 50]. The 2D representation incorporates the geometric properties of a jelly-roll battery cell, which are vital for capturing the complex behaviors of batteries under diverse operational conditions. The necessary battery parameters and initial conditional variables are

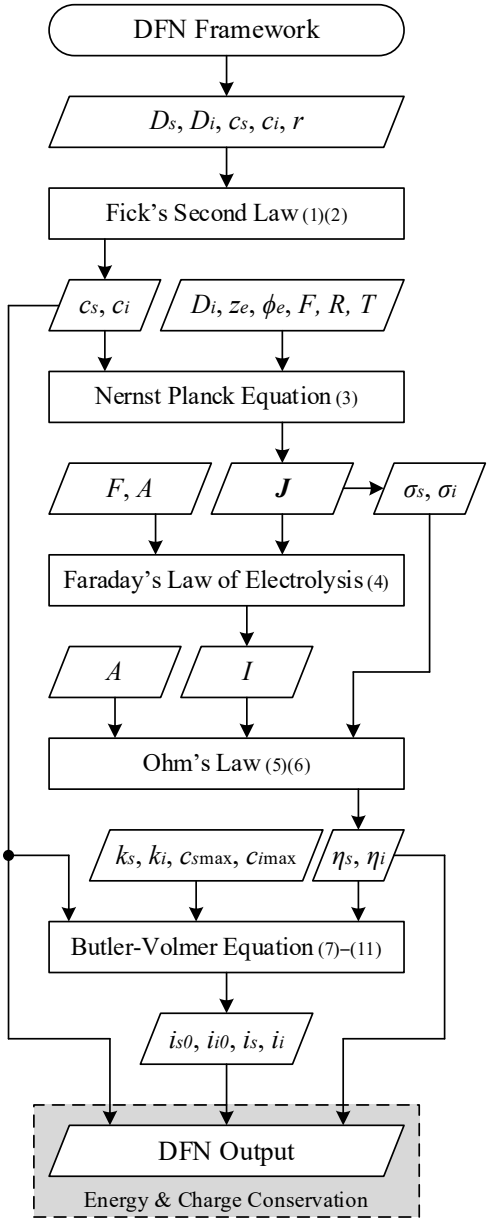

Figure 2: DFN architecture flowchart.

Table 1: List of math symbols and descriptions of parameters and variables that appeared in the modeling process (part 2 of 2).

Class	Symbol	Description	Value	Unit
SEI Layer	d_{SEI}	thickness	(12)(17)(18)	m
	$d_{\text{SEI,ini}}$	initial thickness	[37]	m
	SEI_{α}	growth rate coefficient	[38]	m/s
	SEI_{γ}	J-dependent growth rate	[38]	$m^3/A/s$
	$\text{SEI}_{\varepsilon,x}$	permittivity	[39]	–
	$\text{SEI}_{\rho,x}$	resistivity	[39]	$\Omega \cdot m$
	$\text{SEI}_{\sigma,x}$	conductivity	[40]	S/m
ECM	R_{ohmic}	Ohmic resistance	[41] (fit)	Ω
	L_s	series inductance	[32, 33, 34]	H
	R_{SEI}	SEI layer resistance	(13)(14)	Ω
	C_{SEI}	SEI layer capacitance	(15)(16)	F
	R_{CT}	charge transfer resistance	[42] (fit)	Ω
	C_{DL}	double layer capacitance	[42] (fit)	F
	Z_w	Warburg element	(21)	$\Omega \sqrt{\ }$
	w_{σ}	Warburg coefficient	(22)	$\Omega/\sqrt{s}$
Constant	ε_0	vacuum permittivity	8.854×10^{-12}	F/m
	B_r	Brüggeman coefficient	[43]	–
	$\mathcal{F}$	Faraday constant	96485	C/mol
	R	ideal gas constant	8.314	J/K/mol
	T	test ambient temperature	(sweep)	°C
Subscript x	an/cath	anode / cathode electrode		
	o/r	oxidized- / reduced-reaction		
	p/n	positive / negative		
	s/i	solid / electrolyte		

acquired from [17, 47]. The top-level flowchart of the presented DFN sub-model is shown in Figure 2. This model considers the impact of changes in SEI layer thickness on reaction rate and conductivity. These factors subsequently influence the estimation of diffusion through simulation, enhancing the model's predictive capabilities. Consequentially, the presented model incorporates five key governing theories:

- Fick's second law, in Equations (1)(2);
- Nernst-Planck equation, in Equation (3);
- Ohm's law, in Equations (5)(6);

- Butler-Volmer equation, in Equations (7)–(11);
- Charge conservation and energy conservation.

Appropriate concatenation of these theories is essential for a reasonable battery performance simulation. Firstly, Fick's second law accounts for the solid and electrolyte phase diffusion profiles [14, 51], the concentration gradient drives the diffusion of ions from regions of higher concentration to regions of lower concentration, eventually leading to a non-homogeneous distribution of Li^+'s across the solid and electrolyte phases. In the context of the DFN model of a cylindrical LIB, it can be expressed separately for the solid and electrolyte phases as given by (1) and (2), respectively.

$$\frac{\partial c_s}{\partial t} = \frac{D_s}{r^2} \cdot \frac{\partial}{\partial r}\left(r^2 \frac{\partial c_s}{\partial r}\right) \tag{1}$$

$$\frac{\partial c_i}{\partial t} = D_i \cdot \nabla^2 c_i \tag{2}$$

where t is time, r is the radius of active material particles in the electrodes, c_x and D_x are the concentration and diffusivity, where $x \in \{s, i\}$ for solid or electrolyte phases, and $\nabla^2 c_i$ is the Laplacian operator, which represents the spatial gradient of the concentration at electrolyte [52, 19]. The integration of both reduced and oxidized (redox) processes within the battery is also incorporated in (1) and (2). These processes play a crucial role in modeling the changing concentration and diffusion of Li^+.

Secondly, the Nernst-Planck equation in (3) takes in the ionic conductivity as well as the electrolyte phase concentration profile, which is derived from the output of Fick's second law for migration and diffusion of Li^+ in the electrolyte [53], where z_e is the charge number of the electroactive species [35], $\mathcal{F}$ is the Faraday constant, R is the ideal gas constant, T is the temperature, and $\nabla\phi_e$ is the gradient of the electric potential. The output $\boldsymbol{J}$ is the ionic current density. The negative sign indicates that the direction of the current flow (e^-) is opposite to that of Li^+.

$$\boldsymbol{J} \triangleq -D_i \nabla c_i - \frac{D_i z_e \mathcal{F}}{RT} c_i \nabla \phi_e \tag{3}$$

Immediate next to the Nernst-Planck equation is an intermediate process described by Faraday's law of electrolysis, given in (4). This law establishes that the current I between electrodes is proportional to the change in the ionic current density $\boldsymbol{J}$. Although the current remains constant throughout

the battery, variations in ionic conductivity within the electrolyte σ_i and the solid phase σ_s lead to differences in overpotentials within phases, denoted by η_s for the solid phase and η_i for the electrolyte. These overpotentials are further defined by Ohm's law, as detailed in equations (5) and (6), with A representing the electrode surface area.

$$I = -\frac{A\boldsymbol{J}}{I} \tag{4}$$

$$\eta_s = -\frac{I}{A\sigma_s} \tag{5}$$

$$\eta_i = -\frac{I}{A\sigma_i} \tag{6}$$

The total overpotential of both phases is required to implement the Butler-Volmer equation for exchange current density i_{x0} and interphasal current density i_x [13]. This equation describes the relationship between the voltage difference across an electrode and the electrical current for a simple, uni-molecular redox reaction [54]. Equations (10) and (11) are used to calculate interphasal current density at solid phase and electrolyte. An abridged step-by-step iteration of intermediate variables are provided in (7)–(9), where k_x is the reaction rate constant, $c_{x\max}$ is defined as the maximum concentration, $x \in \{s, i\}$.

$$\eta_{\text{tot}} = \eta_s - \eta_i \tag{7}$$

$$i_{s0} \triangleq k_s \cdot \sqrt{c_{s\max}(1 - c_s)} \cdot \sinh\left(\frac{\mathcal{F}}{2RT}\eta_{\text{tot}}\right) \tag{8}$$

$$i_{i0} \triangleq k_i \cdot \sqrt{c_{i\max}(1 - c_i)} \cdot \sinh\left(\frac{\mathcal{F}}{2RT}\eta_{\text{tot}}\right) \tag{9}$$

$$i_s \triangleq i_{s0} \cdot \sqrt{c_{s\max}c_s} \tag{10}$$

$$i_i \triangleq i_{i0} \cdot \sqrt{c_{i\max}c_i} \tag{11}$$

Last, the laws of charge and energy conservation are incorporated to ensure a zero-sum transport of charge and a balance in energy conversion within the battery model. This is achieved during simulation by cross-checking overpotential and ionic conductivity at each time step, thus maintaining consistency with the fundamental principles of physics. These two parameters directly influence the efficiency of charge transport and energy conversion [55, 56, 57]. The outputs of the presented DFN model are then used in setting up SEI layer model in Section 2.2.

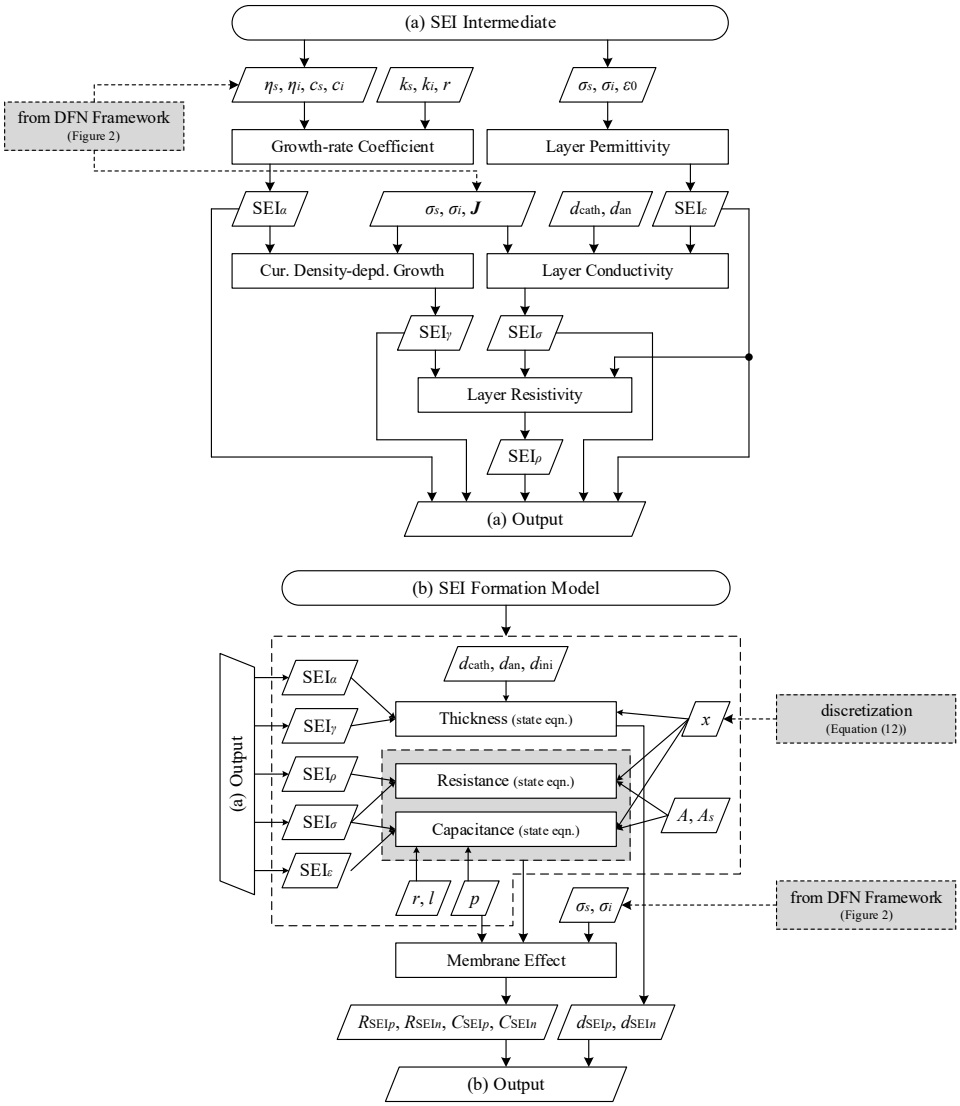

Figure 3: SEI layer formation model flowchart, which mainly consists of two sub-parts: (a) SEI intermediate variables, and (b) SEI formation model for state space equations construction.

2.2. SEI Layer Formation

The SEI formation process is often viewed as a side effect of battery operation. From a modeling standpoint, the DFN model and SEI sub-models are integrated and function in a complementary manner. The SEI layer

formation model is built upon the DFN framework but is not merely an extension of the latter. The purpose behind developing this coupled model is to offer a detailed insight into the battery's operational processes. However, due to the static nature of the model, it focuses on capturing the initial formation of the SEI layer, without exploring the underlying factors that lead to battery degradation and capacity loss. The formation process can be streamlined in terms of essential features of the SEI, by using three common assumptions:

(1) The SEI layer conductivity and electrolyte diffusivity are assumed to be constant, this is justified in [14, 38, 58, 59], allowing a straightforward calculation for fast convergence on battery operation.
(2) The SEI layer accumulation is modeled per *layer* over the electrode surface despite the particle agglomeration effect [58, 60, 61].
(3) Under regular test conditions, the SEI layer is assumed to grow *uniformly* at the entire contacting surface with respect to time [59, 62].

The overall flowchart of the SEI model is shown in Figure 3, where in (a), the model calculates the necessary SEI intermediate variables. The SEI layer growth-rate coefficient SEIα indicates the rate at which the SEI forms on the electrode surface, which is derived from the kinetics of electrochemical reactions and the diffusion of reactants, depending on overpotentials, Li^+ concentration, and reaction rates at both the solid and electrolyte phases [38]. Meanwhile, current density-dependent growth rate SEIγ explains how SEI growth varies with current density, which is calculated by modeling the impact of current density on reaction rates and SEI formation [38].

Furthermore, the permittivity SEIε is calculated to understand the dielectric properties of the SEI, indicating the SEI layer's ability to store electrical energy within an electric field [39]. The conductivity SEIσ measures the easiness of ionic movement through the SEI layer, impacting the battery's overall ionic transport efficiency [40]. Similarly, resistivity SEI_ρ quantifies the SEI layer's resistance to ionic movement, which is crucial for understanding the SEI's impact on battery internal resistance [39].

Based on the works presented in [38, 39, 40], the calculations of these intermediate variables are validated through comparisons with experimental measurements, including electrochemical impedance spectroscopy and direct SEI property measurements, this is to ensure accurate modeling of the SEI layer physical and chemical behavior.

The intermediate variables are then used in the SEI formation model for constructing the state space equations to calculate SEI layer features, namely thickness, resistance, and capacitance (SEI-dRC), this forms a state vector denoted as $[d_{\cdot\text{SEI},p}, d_{\cdot\text{SEI},n}, R_{\cdot\text{SEI},p}, R_{\cdot\text{SEI},n}, C_{\cdot\text{SEI},p}, C_{\cdot\text{SEI},n}]^{\top}$, respectively.

The SEI layer grows on the surface of the anode due to the effect of the Li^+ loss during the reduced reaction at SEI. The model shown in Figure3(b) discretizes the positive and negative electrode in terms of operation time and layer depth, then calculates the layer growth from the initial thickness, growth rate, and position. The discretization process based on the assumptions, the change in thickness Δd_{SEI} can be calculated as –

$$\Delta d_{\text{SEI}}(x,t) = d_{\text{SEI,ini}} + \frac{\mathrm{d}x}{\mathrm{d}t} \cdot \text{SEI}_{\gamma} \tag{12}$$

where x and t are the discretized electrode position and cycling time; $d_{\text{SEI,ini}}$ is the initial thickness [37], and SEI_{γ} is the SEI layer growth rate, which is an intrinsic property based on the membrane material and electrolyte composition, usually determined empirically or fit from experimental observations [38]. The battery under test in this model is a lithium-nickel-manganese-cobalt-oxide ($LiNi_xMn_yCo_{1-x-y}O_2$ or NMC) battery, where SEI_{γ} can vary greatly but typically falls within 5–20 nm/cycle [63]. On the other hand, for lithium-iron-phosphate ($LiFePO_4$ or LFP) batteries, SEI_{γ} was observed to be in the range of 1–5 nm/cycle under certain conditions [64].

Note that the "discretization" process in this context involves breaking down the gradual evolution of the SEI layer growth on the electrode surface into discrete steps. While each step represents a specific moment in time and a specific layer thickness. By doing this, the SEI layer formation can be analyzed step by step, which helps understanding the effect of the SEI layer and its impact on the battery's capacity fade.

The functions computing the SEI-dRC are represented in (13)–(18), where $R_{\text{SEI,disc}}$ and $C_{\text{SEI,disc}}$ are the discretized SEI resistance and capacitance, respectively; σ_x is the electrode conductivity, the SEI_x are several inherent properties of the layer, as provided in Table 1. The subscript x here represents variables associated with either the positive p or negative n electrode.

$$\mathrm{d}\begin{bmatrix} R_{\mathrm{SEI},p} \\ R_{\mathrm{SEI},n} \end{bmatrix} = \begin{bmatrix} \sigma_p d_{\mathrm{SEI},p} \cdot \mathrm{SEI}_{\rho,p} & 0 \\ 0 & \sigma_n d_{\mathrm{SEI},n} \cdot \mathrm{SEI}_{\rho,n} \end{bmatrix} \times \begin{bmatrix} 1 + d_{\mathrm{SEI},p} \cdot \mathrm{SEI}_{\gamma} & 0 \\ 0 & 1 + d_{\mathrm{SEI},n} \cdot \mathrm{SEI}_{\gamma} \end{bmatrix}^{-\mathrm{SEI}_{\alpha}} \times \mathrm{d}\begin{bmatrix} d_{\mathrm{SEI},p} \\ d_{\mathrm{SEI},n} \end{bmatrix} \tag{13}$$

$$R_{\mathrm{SEI,disc}} = R_{\mathrm{SEI},p} + R_{\mathrm{SEI},n} \tag{14}$$

$$\mathrm{d}\begin{bmatrix} C_{\mathrm{SEI},p} \\ C_{\mathrm{SEI},n} \end{bmatrix} = -A\begin{bmatrix} \mathrm{SEI}_{\epsilon,p} & 0 \\ 0 & \mathrm{SEI}_{\epsilon,n} \end{bmatrix} \times \begin{bmatrix} d_{\mathrm{SEI},p}^2 & 0 \\ 0 & d_{\mathrm{SEI},n}^2 \end{bmatrix}^{-1} \times \mathrm{d}\begin{bmatrix} d_{\mathrm{SEI},p} \\ d_{\mathrm{SEI},n} \end{bmatrix} \tag{15}$$

$$C_{\mathrm{SEI,disc}} = \frac{C_{\mathrm{SEI},p} \cdot C_{\mathrm{SEI},n}}{C_{\mathrm{SEI},p} + C_{\mathrm{SEI},n}} \tag{16}$$

$$\mathrm{d}\begin{bmatrix} d_{\mathrm{SEI},p} \\ d_{\mathrm{SEI},n} \end{bmatrix} = \begin{bmatrix} d_{\mathrm{SEI},p,\mathrm{ini}} \\ d_{\mathrm{SEI},n,\mathrm{ini}} \end{bmatrix} + A\boldsymbol{J} \cdot \mathrm{SEI}_{\gamma} \times \mathrm{d}\begin{bmatrix} R_{\mathrm{SEI},p} \\ R_{\mathrm{SEI},n} \end{bmatrix} \tag{17}$$

$$d_{\mathrm{SEI}} = d_{\mathrm{SEI},p} + d_{\mathrm{SEI},n} \tag{18}$$

The thickness of the SEI layer d_{SEI} is directly related to the change in SEI resistance, Li^+ concentration c_s, current density-dependent SEI growth rate SEI_{γ}, and current density i_s. Comprehensive insights into the electrochemical reactions driving SEI layer formation are detailed in previous studies [38, 65]. The SEI resistor is treated physically as the increment in resistance to the flow of Li^+ between the electrode and electrolyte. It subsequently influences the battery's charge transfer efficiency. Note that an increase in SEI resistance yields degraded battery performance, especially in terms of reduced capacity, slower charge rates, and accelerated aging [65, 66]. On the other hand, when calculating SEI capacitance, it is important to consider the permittivity and thickness of the SEI layer [39], as is shown in (15) and (16), describing an interconnected relationship between both electrodes' behaviors. The results are then adjusted by incorporating the Brüggeman coefficient B_r [43].

The overall SEI output is the discretized SEI-dRC with respect to time. At the current state, the model is equipped with prediction ability for battery discharge quantification.

At this point, the two important subparts of the model have been introduced. Note that the model is specifically parameterized based on the intrinsic properties of the battery, with the only geometric constraint being that it must be a cylindrical jelly-roll design. Consequentially, collecting the necessary data for the specific battery becomes a challenging task. However, the parameterization setup ensures that, with carefully selected parameter inputs, the model is scalable and can be applied to any cylindrical jelly-roll battery. In the upcoming sections, it will be demonstrated that the comprehensive model is capable of accurately tracking discharge behavior and characterizing the EIS profile of a specific battery under various conditions.

3. Model Simulation & Validation

The battery selected for the modeling and simulation is the LG MJ1 INR-18650, with its specifications listed in Table 2 and referenced in [23, 24]. The LG MJ1 battery, because of its high energy density and reliable performance, has become a frequently used research subject. The well-documented studies and operation records are publicly accessible, and datasets from various test purposes are readily obtainable. These resources are essential for validating and benchmarking the model [47, 67, 68, 69].

The discharge behaviors of a fresh battery under various charge rates are simulated in MATLAB version 2022b. The processor and operating system used are 4 GHz Quad-Core Intel Core i7, and MacOS Monterey version 12.6.2. The installed memory is 32 GB 1867 MHz DDR3. Figure 4 shows the simulation result for when the charge rate C_{rate} is swept from -1C to -8C (negative sign indicates discharge). The first observation is that, the voltage change over time shows a quasi-linear response from the very beginning of the discharge process, this further corresponds to a constant state-of-charge (SOC) decrement. The slope of the curve is more sensitive to the C_{rate}, where higher discharge rate leads to a steeper voltage drop, whiis is as expected. When $C_{\text{rate}} = -2\text{C}$, the simulation result is in good agreement with the empirical result for the same battery at acceptance reported by Iannello *et al.* [68] and Krause *et al.* [69]. The disagreement in the slope changes between time t_0 and t_1 could be due to variations in the internal resistance, or discrepancies in the environmental conditions during testing.

Another observation is the rapid voltage drop occurring at the "inflection point," as labeled in Figure 4, indicating the voltage cut-off. During battery discharge, Li^+'s move from the anode to the cathode through the electrolyte.

Table 2: LG MJ1 battery specifications.

Parameter	Location	Value	Unit	Reference
size		INR-18650	–	[23]
cathode		NMC-811	–	[23]
anode		silicon graphite	–	[23]
membrane		polyethylene	–	[24]
nom. capacity		3.50	Ah	[23]
nom. voltage		3.635	V	[23]
disch. cutoff volt.		2.50	V	[24]
charge voltage		4.2 ± 0.05	V	[23]
max disch. curr.		10	A	[24]
Brüggeman coeff.		1.5	–	[43]
conductivity	cathode	1.58	S/m	[25]
	anode	1.04	S/m	[25]
	membrane	0.344	S/m	[28]
	electrolyte	1.1	S/m	[25]
diffusivity	cathode	5.35×10^{-7}	m^2/s	[25]
	anode	5.37×10^{-7}	m^2/s	[25]
	membrane	1.68×10^{-7}	m^2/s	[28]
	electrolyte	5.34×10^{-10}	m^2/s	[25]
reaction rate	negative	6.48×10^{-7}	A/m^2	[25]
	positive	3.59×10^{-6}	A/m^2	[25]
Li^+ concentration	negative	33429	mol/m^3	[36]
	positive	63104	mol/m^3	[36]

A higher discharge rate exacerbates the collision of Li^+'s with the cathode's crystal lattice structure, causing the material to undergo distortions or rearrangements [70, 71, 8]. This makes the cathode reach its capacity limit faster. At the inflection point, the cathode reaches its capacity limit and can no longer store more Li^+'s, resulting in a rapid voltage drop. This explains why fast charging/discharging can shorten battery life, as the structural stress on the cathode accelerates degradation.

Note that the voltage response of NMC batteries during discharge only has one inflection point occurring at low SOC. In contrast, LFP batteries

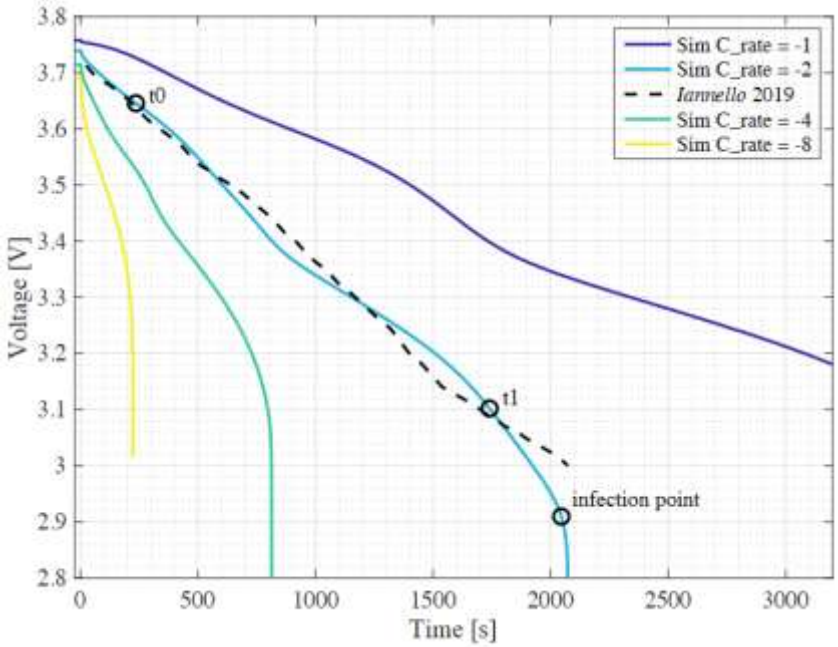

Figure 4: Discharge behaviors of a fresh battery under various charge rates, where the case $C_{\text{rate}} = -2$ is compared against the results in [68, 69].

have a more distinct voltage plateau due to the two-phase reaction in the LFP cathode material [12, 72], thus comparatively the slope of the linear region in LFP batteries is less sensitive to C_{rate} [72, 73].

4. Experiments

After repeated simulation and characterization, the EIS profile for LG MJ1 battery is presented in Figure 5, in the form of the Nyquist plots under variant test ambient temperatures. The x- and y-axes denote the real- and negative-imaginary-part of impedance, respectively.

To begin with, it is observed that the size of EIS arches becomes larger when the temperature changes from 50 to 5°C, presented by the increment at both real- and imaginary-impedance values. This observation is consistent with previous works and results in the literature [22, 74, 75], since the Li^+ diffusion becomes slower at lower temperature values. As per Brownian motion, the reduced kinetic energy of molecules slows down the reactions, therefore leading to increased impedance.

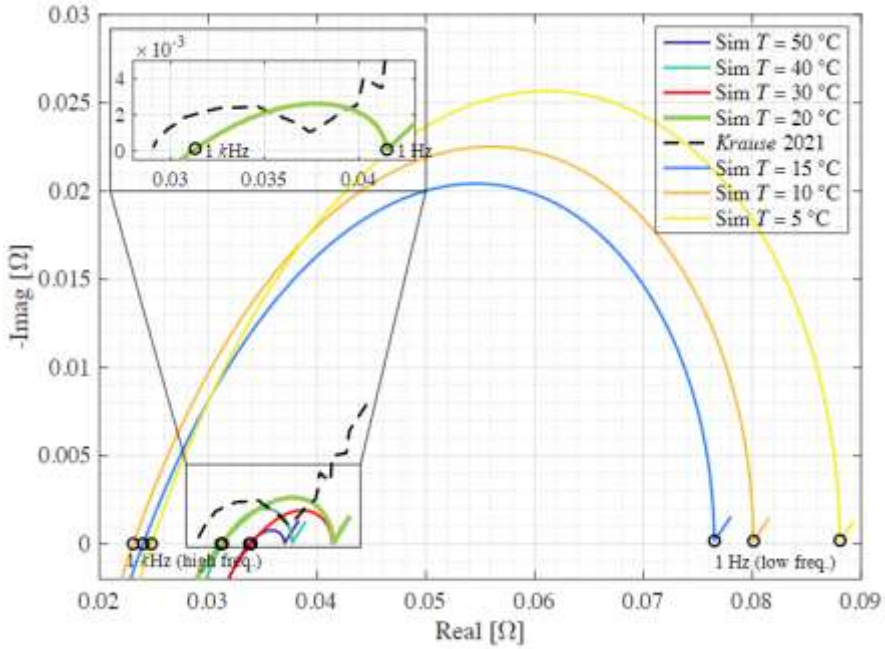

Figure 5: The sweep of EIS of LG MJ1 battery at acceptance, under different test ambient temperatures. The result is compared against the experimental characterization of the same battery. Experimental results © NASA 2019 [68].

Moreover, when T = 20°C, the model shows a good match against NASA EIS qualification [68, 69]. The comparison between simulation and empirical result is zoomed-in at the top-left corner in Figure 5. However, a 5mΩ real impedance offset between the simulated and experimental results is observed. Upon close inspection, this could reasonably be attributed to a few factors such as:

- The simplifications in the SEI model, though necessary, can yield slight differences between the model result and the experimentally measured data.
- Discrepancies could arise from slight differences in the test conditions, under which the simulation is conducted, such as temperature or current rate, when compared to the conditions of NASA's experiments.

The EIS curve provides valuable insights into the electrical properties of the battery under study. One insight is that it can be used to populate the circuit elements within a predefined ECM setup [76]. In Figure 6, a detailed layout of the ECM and a flowchart illustrating the calculation for specific circuit elements are also provided [77]. The ECM comprises four

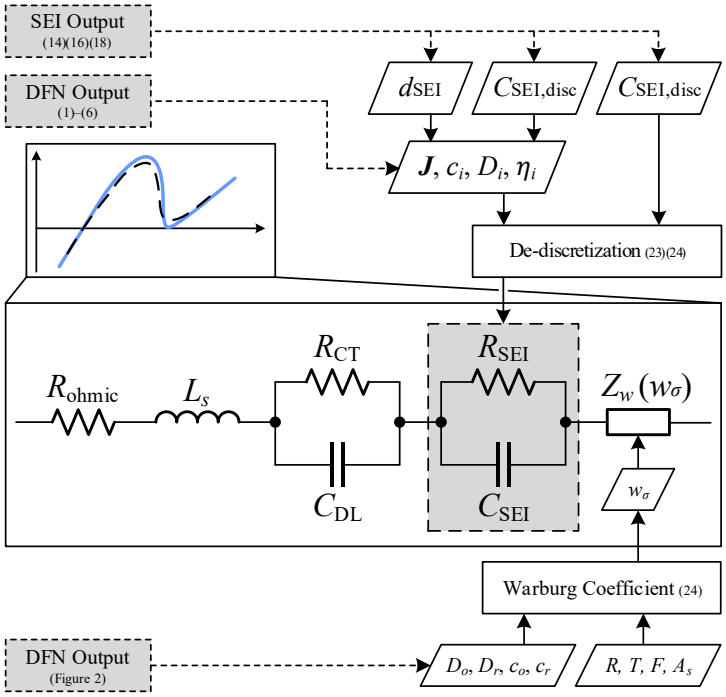

Figure 6: A pre-determined ECM structre of a typical Li-ion battery

primary circuit segments connected in series: 1) a series resistor-inductor (RL) pair, 2) a high-frequency (HF) parallel resistor-capacitor (RC) pair, 3) a low-frequency parallel RC pair, and 4) a Warburg impedance element. These four segments represent various electrochemical processes occurring within the battery during operation.

The series RL represents the ohmic resistance R_{ohmic} and inductive behavior L_s. The ohmic resistance corresponds to the immediate voltage drop when a current is applied to the battery. The inductive behavior of a battery mainly accounts for a small inductive loop attributed to the inductive nature of the current collectors or electromagnetic interactions between battery components, such as cell winding.

The HF parallel RC pair is used to model the charge transfer resistance R_{CT} and the double layer capacitance C_{DL} at the SEI layer. This is a rapid process that incurs instantaneous impedance changes in response to current or voltage variations. Hence, they occur in the high-frequency region of the impedance spectrum, usually in the range of 100Hz to 10kHz [15, 78]. During operation, the charge transfer involves the oxidized or reduced reactions at

the electrode surface, which can be inhibited by this resistance [79, 80]. On the other hand, when a potential is applied across the electrode-electrolyte interphase, the separation of charges creates a capacitive effect, which results in double layer capacitance C_{DL}.

In contrast to the HF response, the parallel SEI RC pair (R_{SEI} and C_{SEI}) is associated with the mass transport processes at the SEI, such as diffusion of Li^+ in the electrode materials, which occur only on slower time scales, thus they become more prominent in the low-frequency spectrum of the EIS profile, typically within the range of 10Hz to 100Hz [9, 10, 39].

In the calculation of this RC pair, the time- and layer position-dependent discretization process in the SEI model prevent their immediate use. Thus, a de-discretization process needs to be performed on both R_{SEI} and C_{SEI}, separately.

The calculation of R_{SEI} employs a dynamic averaged model, involving the selection of a time interval Δt within the linear region of battery discharge response, shown in Figure 4, from t_0 to t_1, while $t_1 - t_0 \geq \Delta t$. A mathematical representation of R_{SEI} de-discretization is shown in (19), where $R_{SEI,tot}$ is the total SEI resistance after the culmination of the said process.

$$R_{\mathrm{SEI,tot}} = \sum_{t=t_0}^{t_1} \left. \frac{\int_{t_0}^{t_0+\Delta t} R_{\mathrm{SEI},d}\,\mathrm{d}t}{\Delta t} \right|_{t_0+\Delta t \leq t_1} \tag{19}$$

In the meantime, the SEI capacitance de-discretization is an accumulative process, addressing spatial and time dependencies, which is closely related to the SEI layer growth process, denoted as d_{SEI}. Revised from [81, 82], for a long-term SEI layer growth, the calculation of $C_{SEI,tot}$ is given in (20).

$$C_{\mathrm{SEI,tot}} = \sqrt{\frac{\boldsymbol{J} \cdot d_{\mathrm{SEI}}}{2c_i D_i \mathcal{F}^2 e^{-\eta_i}} \eta_i^{-1}} \sum_{t=t_0}^{t_1} \left. \int_{t_0}^{t_0+\Delta t} C_{\mathrm{SEI},d}\,\mathrm{d}t \right|_{t_0+\Delta t \leq t_1} \tag{20}$$

In the physical interpretation of battery behavior, the Warburg element Z_w is associated with the time-dependent impedance due to Li^+ diffusion within the electrode material [38, 83]. Since this diffusion process is relatively slow compared to the other electrochemical processes in the battery, its impact on the EIS is more pronounced at lower frequencies below 1 Hz [79]. It's impedance can be calculated by (21).

$$Z_w(w_\sigma) = \frac{w_\sigma}{\sqrt{2\pi f}}(1 - j) \tag{21}$$

where w_σ is the Warburg coefficient. The value of which can be calculated from the redox processes within the battery given in (22), where D and c are the diffusivity and concentration coefficients with subscripts o and r for oxidation or reduction reactions, respectively.

$$w_\sigma = \frac{RT}{\sqrt{2}A_s^2\mathcal{F}^2}\left(\frac{1}{\sqrt{D_o}c_o} + \frac{1}{\sqrt{D_r}c_r}\right) \tag{22}$$

With properly quantified circuit elements $\{R_{\text{SEI,tot}}, C_{\text{SEI,tot}}, w_\sigma\}$, the remainder components in the ECM are then curve-fitted from the EIS result in Figure 5, when T = 20°C. The ECM fitting process utilizes nonlinear multivariable optimization function, searching for minimum value specified as $\min_x \mathsf{L}$, where L is the cost function defined as the sum of root-mean-square error of difference between the fitted and simulated EIS. The process constructing L is described as follows –

(1) Given quantified $\{R_{\text{SEI,tot}}, C_{\text{SEI,tot}}, w_\sigma\}$;
(2) Given frequency range f = [0.1, $3k$] Hz;
(3) Initial guess $\{R_{\text{ohmic}}, L_s, R_{\text{CT}}, C_{\text{DL}}\}$;
(4) Calculate total frequency-domain impedance Z_{tot} in (23), where s is Laplace transform operator, $\text{s} \triangleq j \cdot 2\pi f$;

$$Z_{\text{tot}} = R_{\text{ohmic}} + \text{s}L_s + \frac{R_{\text{CT}} \cdot \frac{1}{sC_{\text{DL}}}}{R_{\text{CT}} + \frac{1}{sC_{\text{DL}}}} + \frac{R_{\text{SEI}} \cdot \frac{1}{sC_{\text{SEI}}}}{R_{\text{SEI}} + \frac{1}{sC_{\text{SEI}}}} + Z_w \tag{23}$$

(5) Construct the cost function L in (24), where Z_{sim} is the simulated total impedance, which is given in Figure 5; num(f) returns the number of elements in frequency vector f.

$$L = \sqrt{\frac{\Sigma^{\text{num}(f)}(Z_{\text{tot}} - Z_{\text{sim}})^2}{\text{num}(f)}} \tag{24}$$

After careful fitting and characterization, the populated ECM component values are listed in Table 3. Note that since the impedance Z_w is frequency-dependent, it is more reasonable to list the Warburg coefficient as the result in ECM.

Table 3: Estimated circuit elements of the predetermined ECM.

Parameter	Value	Unit	Calculation
L_s	29.56	μH	curvefit
R_{ohmic}	5.85	mΩ	curvefit
R_{SEI}	12.84	mΩ	(19)
C_{SEI}	0.19	F	(20)
R_{CT}	23.78	mΩ	curvefit
C_{DL}	34.98	mF	curvefit
w_σ	56.91	$\mu\Omega/\sqrt{s}$	(22)

5. Conclusion

In this paper, a physics-based LIB mathematical model is presented in details, regarding the different sub-models including DFN framework, SEI layer formation, and ECM population. The novelty of this approach is to enable the derivation of ECM circuit components directly from the battery's physical properties. The simulation and characterization of battery discharging behavior and EIS profile under diverse conditions are presented with validation comparing to NASA's empirical data [68, 69]. This proves the accuracy and predictive capabilities of the presented model. The interaction between the physical model and the ECM captures the battery's real-time behavior in both time- and frequency-domains. The ECM parameters and EIS data provide valuable insight into the electrical properties of the battery under study. This information is crucial for understanding the battery's behavior under different operating conditions and developing effective battery management strategies. Although not exhaustive, the model is adaptable for tracking battery operation status. It also paves the way for future studies to focus on visualizing degradation mechanisms and evaluating state of health, contributing to enhanced battery performance and longevity.

Data Availability

Data will be made available on request.

Acknowledgments

This material is based upon work supported in part (for author Jaber A. Abu Qahouq) by the National Science Foundation (NSF, United States) under Grant No. 2213918. Any opinions, findings and conclusions or recommendations expressed in this material are those of the authors and do not necessarily reflect the views of the NSF.

The Center for Advanced Vehicle Technologies (CAVT) of The University of Alabama – Tuscaloosa has supported in part (for author Jin Zhao) to carry out this work. Any opinions, findings and conclusions or recommendations expressed in this material are those of the authors and do not necessarily reflect the views of CAVT.

References

[1] X. Zhao, S. Liu, E. Li, Z. Wang, F. Gu, A. D. Ball, A hybrid intelligent model using the distribution of relaxation time analysis of electrochemical impedance spectroscopy for lithium-ion battery state of health estimation, Journal of Energy Storage 84 (2024) 110814.

[2] C. Lv, X. Zhou, L. Zhong, C. Yan, M. Srinivasan, Z. W. Seh, C. Liu, H. Pan, S. Li, Y. Wen, et al., Machine learning: an advanced platform for materials development and state prediction in lithium-ion batteries, Advanced Materials 34 (2022) 2101474.

[3] M.-K. Tran, S. Panchal, V. Chauhan, N. Brahmbhatt, A. Mevawalla, R. Fraser, M. Fowler, Python-based scikit-learn machine learning models for thermal and electrical performance prediction of high-capacity lithium-ion battery, International Journal of Energy Research 46 (2022) 786–794.

[4] J. Schmitt, I. Horstkötter, B. Bäker, Electrical lithium-ion battery models based on recurrent neural networks: A holistic approach, Journal of Energy Storage 58 (2023) 106461.

[5] W. Huang, J. A. A. Qahouq, Small-signal modeling and controller design of energy sharing controlled distributed battery system, Simulation Modelling Practice and Theory 77 (2017) 1–19.

[6] P. Kollmeyer, A. Hackl, A. Emadi, Li-ion battery model performance for automotive drive cycles with current pulse and eis parameterization, in: 2017 IEEE transportation electrification conference and expo (ITEC), IEEE, 2017, pp. 486–492.

[7] J. A. A. Qahouq, Z. Xia, Single-perturbation-cycle online battery impedance spectrum measurement method with closed-loop control of power converter, IEEE Transactions on Industrial Electronics 64 (2017) 7019–7029.

[8] M. Fang, X. Yue, Y. Dong, Y. Chen, Z. Liang, A temperature-dependent solvating electrolyte for wide-temperature and fast-charging lithium metal batteries, Joule 8 (2024) 91–103.

[9] M. Naguib, C. Vidal, P. Kollmeyer, P. Malysz, O. Gross, A. Emadi, Comparative study between equivalent circuit and recurrent neural network battery voltage models, SAE Technical Paper 1 (2021) 759.

[10] C. Li, N. Cui, Z. Cui, C. Wang, C. Zhang, Novel equivalent circuit model for high-energy lithium-ion batteries considering the effect of nonlinear solid-phase diffusion, Journal of Power Sources 523 (2022) 230993.

[11] S. Han, Y. Tang, S. K. Rahimian, A numerically efficient method of solving the full-order pseudo-2-dimensional (p2d) li-ion cell model, Journal of Power Sources 490 (2021) 229571.

[12] A. J. Crawford, D. Choi, P. J. Balducci, V. R. Subramanian, V. V. Viswanathan, Lithium-ion battery physics and statistics-based state of health model, Journal of Power Sources 501 (2021) 230032.

[13] E. Paccha-Herrera, W. R. Calderón-Muñoz, M. Orchard, F. Jaramillo, K. Medjaher, Thermal modeling approaches for a licoo2 lithium-ion battery—a comparative study with experimental validation, Batteries 6 (2020) 40.

[14] M. Doyle, T. F. Fuller, J. Newman, Modeling of galvanostatic charge and discharge of the lithium/polymer/insertion cell, Journal of the Electrochemical society 140 (1993) 1526.

[15] S. B. Lee, S. Onori, A robust and sleek electrochemical battery model implementation: a matlab® framework, Journal of The Electrochemical Society 168 (2021) 090527.

[16] V. Sulzer, S. G. Marquis, R. Timms, M. Robinson, S. J. Chapman, Python battery mathematical modelling (pybamm), Journal of Open Research Software 9 (2021).

[17] A. Wang, S. O'Kane, F. B. Planella, J. Le Houx, K. O'Regan, M. Zyskin, J. Edge, C. Monroe, S. Cooper, D. A. Howey, et al., Review of parameterisation and a novel database (liiondb) for continuum li-ion battery models, Progress in Energy 4 (2022) 032004.

[18] H. Tu, S. Moura, Y. Wang, H. Fang, Integrating physics-based modeling with machine learning for lithium-ion batteries, Applied Energy 329 (2023) 120289.

[19] M. Lagnoni, C. Nicolella, A. Bertei, Comparison of electrolyte transport modelling in lithium-ion batteries: concentrated solution theory vs generalized nernst-planck model, Journal of The Electrochemical Society 169 (2022) 020570.

[20] T. Chen, S. Kornblith, M. Norouzi, G. Hinton, A simple framework for contrastive learning of visual representations, in: International conference on machine learning, PMLR, 2020, pp. 1597–1607.

[21] W.-J. Lin, K.-C. Chen, Evolution of parameters in the doyle-fuller-newman model of cycling lithium ion batteries by multi-objective optimization, Applied Energy 314 (2022) 118925.

[22] X. He, D. Bresser, S. Passerini, F. Baakes, U. Krewer, J. Lopez, C. T. Mallia, Y. Shao-Horn, I. Cekic-Laskovic, S. Wiemers-Meyer, et al., The passivity of lithium electrodes in liquid electrolytes for secondary batteries, Nature Reviews Materials 6 (2021) 1036–1052.

[23] Product Specification: Rechargeable Lithium Ion Battery Model INR18650 MJ1 3500mAh, LG Chemical MBD/MBDC Ltd., Seoul, Korea, 2014. (Accessed on 5/2/2023).

[24] Material Safety Data Sheet: INR18650 Lithium-Ion Battery, LG Chemical MBD/MBDC Ltd., Seoul, Korea, 2016. (Accessed on 5/2/2023).

[25] O. Chaouachi, J.-M. Réty, S. Génies, M. Chandesris, Y. Bultel, Experimental and theoretical investigation of li-ion battery active materials properties: Application to a graphite/ni0. 6mn0. 2co0. 2o2 system, Electrochimica Acta 366 (2021) 137428.

[26] W. Waag, S. Käbitz, D. U. Sauer, Experimental investigation of the lithium-ion battery impedance characteristic at various conditions and aging states and its influence on the application, Applied energy 102 (2013) 885–897.

[27] J. Y. Kim, D. O. Shin, T. Chang, K. M. Kim, J. Jeong, J. Park, Y. M. Lee, K. Y. Cho, C. Phatak, S. Hong, et al., Effect of the dielectric constant of a liquid electrolyte on lithium metal anodes, Electrochimica Acta 300 (2019) 299–305.

[28] J. Landesfeind, J. Hattendorff, A. Ehrl, W. A. Wall, H. A. Gasteiger, Tortuosity determination of battery electrodes and separators by impedance spectroscopy, Journal of The Electrochemical Society 163 (2016) A1373.

[29] Z. Stojek, The electrical double layer and its structure, Electroanalytical methods: Guide to experiments and applications (2010) 3–9.

[30] Q. Wu, M. T. McDowell, Y. Qi, Effect of the electric double layer (edl) in multicomponent electrolyte reduction and solid electrolyte interphase (sei) formation in lithium batteries, Journal of the American Chemical Society 145 (2023) 2473–2484.

[31] X. Wu, X. Jiang, Z. Ye, Y. Zeng, C. Lv, Copper foil after hydrothermal treatment in acidified tungstate solution as conductor-and binder-free anode electrodes for high performance lithium-ion batteries, Instrumentation Science & Technology 50 (2022) 437–446.

[32] H. Dai, B. Jiang, X. Wei, Impedance characterization and modeling of lithium-ion batteries considering the internal temperature gradient, Energies 11 (2018) 220.

[33] M. Gaberšček, Understanding li-based battery materials via electrochemical impedance spectroscopy, Nature Communications 12 (2021) 6513.

[34] A. Urban, D.-H. Seo, G. Ceder, Computational understanding of li-ion batteries, npj Computational Materials 2 (2016) 1–13.

[35] P. Kissinger, W. R. Heineman, Laboratory Techniques in Electroanalytical Chemistry, revised and expanded, CRC press, 2018.

[36] J. Schmalstieg, C. Rahe, M. Ecker, D. U. Sauer, Full cell parameterization of a high-power lithium-ion battery for a physico-chemical model: Part i. physical and electrochemical parameters, Journal of The Electrochemical Society 165 (2018) A3799.

[37] J. Lei, L. Li, R. Kostecki, R. Muller, F. McLarnon, Characterization of sei layers on limn2o4 cathodes with in situ spectroscopic ellipsometry, Journal of the Electrochemical Society 152 (2005) A774.

[38] S. K. M. Reddy, W. Shang, R. E. White, Mathematical model for sei growth under open-circuit conditions, Journal of The Electrochemical Society 169 (2022) 090505.

[39] A. Wang, S. Kadam, H. Li, S. Shi, Y. Qi, Review on modeling of the anode solid electrolyte interphase (sei) for lithium-ion batteries, npj Computational Materials 4 (2018) 15.

[40] S. Das, P. M. Attia, W. C. Chueh, M. Z. Bazant, Electrochemical kinetics of sei growth on carbon black: Part ii. modeling, Journal of The Electrochemical Society 166 (2019) E107–E118.

[41] U. Morali, S. Erol, Analysis of electrochemical impedance spectroscopy response for commercial lithium-ion batteries: modeling of equivalent circuit elements, Turkish Journal of Chemistry 44 (2020) 602–613.

[42] N. Meddings, M. Heinrich, F. Overney, J.-S. Lee, V. Ruiz, E. Napolitano, S. Seitz, G. Hinds, R. Raccichini, M. Gaberšček, et al., Application of electrochemical impedance spectroscopy to commercial li-ion cells: A review, Journal of Power Sources 480 (2020) 228742.

[43] C.-H. Chen, F. B. Planella, K. O'regan, D. Gastol, W. D. Widanage, E. Kendrick, Development of experimental techniques for parameterization of multi-scale lithium-ion battery models, Journal of The Electrochemical Society 167 (2020) 080534.

[44] A. Wang, S. O'Kane, F. B. Planella, J. Le Houx, K. O'Regan, M. Zyskin, J. Edge, C. Monroe, S. Cooper, D. A. Howey, et al., Dfn parameter database, 2022. URL: https://liiondb.com/, (Accessed on 9/13/2023).

[45] T. M. Heenan, A. Jnawali, M. Kok, T. G. Tranter, C. Tan, A. Dimitrijevic, R. Jervis, D. Brett, P. Shearing, Lithium-ion battery inr18650 mj1 data: 400 electrochemical cycles (eil-015), 2020. URL: https://rdr.ucl.ac.uk/articles/dataset/Lithium-ion_Battery_INR18650_MJ1_Data_400_Electrochemical_Cycles_EIL-015_/12159462, (Accessed on 12/8/2023).

[46] NASA's Open Data Portal, Li-ion battery aging datasets, 2022. URL: https://data.nasa.gov/dataset/Li-ion-Battery-Aging-Datasets/uj5r-zjdb/about_data, (Accessed on 3/13/2024).

[47] G. Dos Reis, C. Strange, M. Yadav, S. Li, Lithium-ion battery data and where to find it, Energy and AI 5 (2021) 100081.

[48] M. A. Rahman, S. Anwar, A. Izadian, Electrochemical model parameter identification of a lithium-ion battery using particle swarm optimization method, Journal of Power Sources 307 (2016) 86–97.

[49] F. B. Planella, M. Sheikh, W. D. Widanage, Systematic derivation and validation of a reduced thermal-electrochemical model for lithium-ion batteries using asymptotic methods, Electrochimica Acta 388 (2021) 138524.

[50] A. Zülke, I. Korotkin, J. M. Foster, M. Nagarathinam, H. Hoster, G. Richardson, Parametrisation and use of a predictive dfn model for a high-energy nca/gr-siox battery, Journal of The Electrochemical Society 168 (2021) 120522.

[51] J. Kim, H. Chun, J. Baek, S. Han, Parameter identification of lithium-ion battery pseudo-2-dimensional models using genetic

algorithm and neural network cooperative optimization, Journal of Energy Storage 45 (2022) 103571.

[52] R. Xiong, H. He, H. Guo, Y. Ding, Modeling for lithium-ion battery used in electric vehicles, Procedia Engineering 15 (2011) 2869–2874.

[53] H. Berg, Batteries for electric vehicles: materials and electrochemistry, Cambridge university press, 2015.

[54] K. Kendall, M. Kendall, S. Adler, Sources of cell and electrode polarisation losses in sofcs, High-Temperature Solid Oxide Fuel Cells 21st Century; Elsevier: London, UK (2016) 357–381.

[55] G. Richardson, I. Korotkin, Heat generation and a conservation law for chemical energy in li-ion batteries, Electrochimica Acta 392 (2021) 138909.

[56] F. Brosa Planella, W. Ai, A. M. Boyce, A. Ghosh, I. Korotkin, S. Sahu, V. Sulzer, R. Timms, T. G. Tranter, M. Zyskin, et al., A continuum of physics-based lithium-ion battery models reviewed, Progress in Energy 4 (2022) 042003.

[57] L. Ding, X. Yue, X. Zhang, Y. Chen, J. Liu, Z. Shi, Z. Wang, X. Yan, Z. Liang, A polyimine aerogel separator with electron cloud design to boost li-ion transport for stable li metal batteries, Proceedings of the National Academy of Sciences 120 (2023) e2314264120.

[58] L. Liu, M. Zhu, Modeling of sei layer growth and electrochemical impedance spectroscopy response using a thermal-electrochemical model of li-ion batteries, ECS Transactions 61 (2014) 43.

[59] COMSOL Inc., Battery design module user's guide, version 5.6, 2023. URL: https://doc.comsol.com/5.6/doc/com.comsol.help.battery/BatteryDesignModuleUsersGuide.pdf, (Accessed on 5/2/2023).

[60] A. Heidarian, S. C. Cheung, R. Ojha, G. Rosengarten, Effects of current collector shape and configuration on charge percolation and electric conductivity of slurry electrodes for electrochemical systems, Energy 239 (2022) 122313.

[61] Y. Ali, N. Iqbal, S. Lee, Role of sei layer growth in fracture probability in lithium-ion battery electrodes, International Journal of Energy Research 45 (2021) 5293–5308.

[62] C. Weng, J. Sun, H. Peng, A unified open-circuit-voltage model of lithium-ion batteries for state-of-charge estimation and state-of-health monitoring, Journal of power Sources 258 (2014) 228–237.

[63] A. Sarkar, I. C. Nlebedim, P. Shrotriya, Performance degradation due to anodic failure mechanisms in lithium-ion batteries, Journal of Power Sources 502 (2021) 229145.

[64] N. Damay, C. Forgez, M.-P. Bichat, G. Friedrich, Thermal modeling of large prismatic lifepo4/graphite battery. coupled thermal and heat generation models for characterization and simulation, Journal of Power Sources 283 (2015) 37–45.

[65] S. J. An, J. Li, C. Daniel, D. Mohanty, S. Nagpure, D. L. Wood III, The state of understanding of the lithium-ion-battery graphite solid electrolyte interphase (sei) and its relationship to formation cycling, Carbon 105 (2016) 52–76.

[66] D. Bresser, S. Passerini, B. Scrosati, Recent progress and remaining challenges in sulfur-based lithium secondary batteries–a review, Chemical communications 49 (2013) 10545–10562.

[67] T. M. Heenan, A. Jnawali, M. Kok, T. G. Tranter, C. Tan, A. Dimitrijevic, R. Jervis, D. Brett, P. Shearing, An advanced microstructural and electrochemical datasheet on 18650 li-ion batteries with nickel-rich nmc811 cathodes and graphite-silicon anodes, Journal of The Electrochemical Society 167 (2020) 140530.

[68] C. Iannello, E. Darcy, E. Brandon, J.-P. Ruiz, K. Billings, C. Krause, R. Bugga, Performance of commercial high energy and high power li-ion cells in jovian missions encountering high radiation environments, NASA Technical Reports Server (2019).

[69] F. Krause, J. Ruiz, S. Jones, E. Brandon, E. Darcy, C. Iannello, R. Bugga, Performance of commercial li-ion cells for future nasa missions and aerospace applications, Journal of The Electrochemical Society 168 (2021) 040504.

[70] H. Tan, H. L. Smith, L. Kim, T. K. Harding, S. C. Jones, B. Fultz, Electrochemical cycling and lithium insertion in nanostructured fef3 cathodes, Journal of The Electrochemical Society 161 (2014) A445.

[71] X. Zhao, X. Tang, L. Zhang, M. Zhao, J. Zhai, Effects of neodymium aliovalent substitution on the structure and electrochemical performance of lifepo4, Electrochimica acta 55 (2010) 5899–5904.

[72] S. N. Islam, S. Saha, M. E. Haque, M. A. Mahmud, Comparative analysis of commonly used batteries for residential solar pv applications, in: 2019 IEEE PES Asia-Pacific Power and Energy Engineering Conference (APPEEC), IEEE, 2019, pp. 1–5.

[73] P. Kurzweil, W. Scheuerpflug, State-of-charge monitoring and battery diagnosis of different lithium ion chemistries using impedance spectroscopy, Batteries 7 (2021) 17.

[74] N. Ogihara, S. Kawauchi, C. Okuda, Y. Itou, Y. Takeuchi, Y. Ukyo, Theoretical and experimental analysis of porous electrodes for lithium-ion batteries by electrochemical impedance spectroscopy using a symmetric cell, Journal of The Electrochemical Society 159 (2012) A1034.

[75] A. Farmann, W. Waag, D. U. Sauer, Adaptive approach for on-board impedance parameters and voltage estimation of lithium-ion batteries in electric vehicles, Journal of power sources 299 (2015) 176–188.

[76] S. D. Talian, S. Brutti, M. A. Navarra, J. Moškon, M. Gaberscek, Impedance spectroscopy applied to lithium battery materials: good practices in measurements and analyses, Energy Storage Materials (2024) 103413.

[77] B. O. Agudelo, W. Zamboni, E. Monmasson, G. Spagnuolo, Identification of battery circuit model from eis data, in: JCGE-Congrès des Jeunes Chercheurs en Génie Electrique, 2019.

[78] J. Zhang, P. Wang, Y. Liu, Z. Cheng, Variable-order equivalent circuit modeling and state of charge estimation of lithium-ion battery based on electrochemical impedance spectroscopy, Energies 14 (2021) 769.

[79] O. Capron, R. Gopalakrishnan, J. Jaguemont, P. Van Den Bossche, N. Omar, J. Van Mierlo, On the ageing of high energy lithium-ion batteries—comprehensive electrochemical diffusivity studies of harvested nickel manganese cobalt electrodes, Materials 11 (2018) 176.

[80] W. Huang, J. A. A. Qahouq, An online battery impedance measurement method using dc–dc power converter control, IEEE Transactions on Industrial Electronics 61 (2014) 5987–5995.

[81] L. von Kolzenberg, A. Latz, B. Horstmann, Solid–electrolyte interphase during battery cycling: Theory of growth regimes, ChemSusChem 13 (2020) 3901–3910.

[82] X. Duan, B. Li, J. Li, X. Gao, L. Wang, J. Xu, Quantitative understanding of lithium deposition-stripping process on graphite anodes of lithium-ion batteries, Advanced Energy Materials 13 (2023) 2203767.

[83] F. Brosa Planella, W. Dhammika Widanage, Systematic derivation of a single particle model with electrolyte and side reactions (spme+ sr) for degradation of lithium-ion batteries, arXiv e-prints (2022) arXiv–2206.